Journal of Hydrology 541 (2016) 344–358

Contents lists available at ScienceDirect

Journal of Hydrology

journal homepage: www.elsevier.com/locate/jhydrol

Modelling large floating bodies in urban area flash-floods via a Smoothed Particle Hydrodynamics model

Raffaele Albano [a,*], Aurelia Sole [a], Domenica Mirauda [a], Jan Adamowski [b]

[a] School of Engineering, University of Basilicata, Italy
[b] Department of Bioresource Engineering, McGill University, Canada

ARTICLE INFO

Article history:
Available online 13 February 2016

Keywords:
Smoothed Particle Hydrodynamics
Floating bodies transport
Flash-flood
Structural mitigation action
Lagrangian modelling
Fluid–structure interaction

SUMMARY

Large debris, including vehicles parked along floodplains, can cause severe damage and significant loss of life during urban area flash-floods. In this study, the authors validated and applied the Smoothed Particle Hydrodynamics (SPH) model, developed in Amicarelli et al. (2015), which reproduces in 3D the dynamics of rigid bodies driven by free surface flows, to the design of flood mitigation measures. To validate the model, the authors compared the model's predictions to the results of an experimental setup, involving a dam breach that strikes two fixed obstacles and three transportable floating bodies. Given the accuracy of the results, in terms of water depth over time and the time history of the bodies' movements, the SPH model explored in this study was used to analyse the mitigation efficiency of a proposed structural intervention – the use of small barriers (groynes) to prevent the transport of floating bodies. Different groynes configurations were examined to identify the most appropriate design and layout for urban area flash-flood damage mitigation. The authors found that groynes positioned upstream and downstream of each floating body can be effective as a risk mitigation measure for damage resulting from their movement.

1. Introduction

Many obstacles may be present in rivers during urban flood events, in both the main channel (bridge piers) and on the floodplains (e.g. abutments, dikes, trees and vegetation, and debris from former floods). Moreover, if river embankments are overcome, or flood dikes breached, the flow will enter areas that are normally not subject to inundation and are therefore not prepared to support such events. These areas generally contain a multitude of other obstacles: roads, vehicles, railways, dwellings, and industrial and commercial structures. The presence of these artificial obstacles can considerably affect water flows. Furthermore, in the event of severe and rapid floods (e.g. flash-floods), the influence of such obstacles is amplified, especially in urban environments. Large debris flow can clog natural sections, forming "debris dams" or "valley jams." In turn, debris dams can contribute to increased water levels up-stream and can cause dam-break flows in the event a sudden breach of large impounded water volumes. These potential impacts are similar to the impacts of temporary dams created by landslide deposits (Lucìa et al., 2015).

Large floating debris transported by the floodwater flow can significantly worsen the effects of flooding by blocking fluvial and road infrastructures and increasing water levels. For example, during the Boscastle flood in England in August 2004, 115 vehicles were swept away by floodwater; some of these vehicles were caught under a local bridge, thereby blocking the flow path and ultimately contributing to the collapse of the bridge due to stress (Teo et al., 2012). Furthermore, during the Rapid City flash flood in South Dakota, USA, on June 9, 1972, 38 cm of precipitation accumulated in less than six hours. As a result, Rapid Creek rose 3.66 m after the spillway at Pactola Dam, located upstream of Rapid Creek, became blocked with cars and house debris (Gruntfest and Ripps, 2000). Large debris, including vehicles parked along floodplains, can cause severe damage and significant loss of life. For example, a high rate of mortality associated with vehicles and floods was documented in the 1976 Big Thompson flood in Colorado, USA (Gruntfest, 1997, 2000).

Computational Fluid Dynamics (CFD) modelling for urban flood events is very useful for characterizing the complexity of an urban system. It also allows for a detailed evaluation and understanding of phenomena such as the transport of solid structures (e.g. vehicles and tree trunks). Accordingly, CFD enables one to perform numerical experiments, rather than expensive and, in some cases, impossible physical experiments, where similarity principles cannot be invoked and scale models cannot be used (Violeau, 2012).

* Corresponding author.
E-mail address: albano.raffaele@tiscali.it (R. Albano).

http://dx.doi.org/10.1016/j.jhydrol.2016.02.009
0022-1694/

CFD modelling also provides additional information that cannot be obtained from direct experimental observation. This is particularly valuable when the aim of the study is not only to describe a flow variable, but rather to understand the physical process controlling the phenomena (Violeau, 2012).

The use of mesh-free methods for CFD has grown exponentially during the last decade. These methods, whose main idea is to substitute the grid by a set of arbitrarily distributed nodes, are expected to be more adaptable and versatile than the conventional grid-based approaches, especially for those applications with severe discontinuities in the fluid. In this context, the Smoothed Particle Hydrodynamics (SPH) model represents a mesh-less CFD technique to simulate free surface and flow impact on fixed and mobile structures and multi-phase flow modelling (Monaghan, 2005; Liu et al., 2013; Vaughan, 2009). It is particularly appropriate for the representation of dynamical flood events, such as urban floods involving obstacles or dam-break conditions, both in terms of their dynamics and with regards to the forecast of their effects (Viccione and Bovolin, 2011).

The main advantages of this technique concern (1) the direct estimation of the free-surface and the interfaces between fluids or phases, as defined by the positions of the numerical particles; (2) the effective management of multiple moving bodies or the transported particle matter; and (3) the computation of Lagrangian parameters and derivatives, avoiding the direct treatment of the non-linear advective term in the Navier–Stokes equation (Gómez-Gesteira and Dalrymple, 2004; Liu and Liu, 2003). Furthermore, the algorithm is rather simple when compared to Eulerian modelling since it requires neither iterative convergence procedures, nor a computational mesh. In particular, this technique provides the greatest advantage when applied to fast flows in transitory regimes. On the other hand, SPH is generally more time-consuming than Eulerian CFD techniques since the numerical stencil of each computational node is composed of approximately one hundred particles in 3D, rather than a tenth of cells for mesh-based models (Viccione et al., 2008). Still, the algorithm is appropriate for parallelization, noticeably reducing the negative effects of this shortcoming (Gomez-Gesteira et al., 2010; Violeau, 2012). Conceptually, the method uses integral theory to transform the partial differential equations into an integral form. Moreover, the SPH approach can simultaneously deal with multiple body dynamics, as are usually developed in astrophysics and solid mechanics (Monaghan, 2005; Liu and Liu, 2003; Violeau, 2012). To date, only a few SPH models have been developed to represent the transport of moving bodies driven by 3D free surface flows. The main difficulties stem from the treatment of each of the multiple 2-way fluid–body and solid–solid (body–body and body–boundary) interactions.

Monaghan et al. (2003) described a SPH numerical method based on boundary force particles in order to model the impact and entry of a rigid body travelling down a slope into water. Using the same technique, Omidvar et al. (2012a,b) investigated the impact of a float device in free-surface waves. The reliability of the boundary force particles technique in reproducing 2D modular bodies in confined flows was highlighted by Kajtar and Monaghan (2010) and later coupled with repulsive forces to model the body force owing to rigid boundaries, (Kajtar and Monaghan, 2012). Hashemi et al. (2011) simulated 2D moving solid bodies in viscoelastic fluid flows through a modified boundary treatment, the Weakly Compressible Smoothed Particle Hydrodynamics technique (WC-SPH), which facilitates the efficient calculation of hydrodynamic forces in multi-body problems. In addition, consistent spatial derivative schemes were used along with a modified mass conservation equation in order to alleviate the need for artificial viscosity and/or artificial stress. Hashemi et al. (2012) and Anghileri et al. (2011) used a coupled (Finite Element Method) FE/SPH approach in order to model the 3D high-velocity impacts that involve fluid–structure interaction. Seungtaik et al. (2009) used an impulse-based boundary force technique to simulate the interaction between body–body in 3D. Both Bouscasse et al. (2013) and Ren et al. (2015) developed Weakly-Compressible SPH models for the non-linear interactions between surface waves and floating bodies. Bouscasse et al. (2013) implemented a ghost-fluid technique, which imposes no-slip conditions on the solid walls. Ren et al. (2015) defined an improved boundary treatment scheme based on "dynamic boundary particles". More recently, Liu et al. (2014) presented a SPH–RANS model for the interaction of free surface flows with moving rigid bodies. The model is validated on several test cases involving the dynamics of a solid cylinder in a free surface flow. Ren et al. (2014) represented the 2D fluid–structure interactions of surface waves and breakwaters using a coupled numerical solution SPH–DEM (Discrete-Element Method). Finally, Sun et al. (2015) developed a SPH model for fluid–structure interactions also with moving boundaries and they implemented an improved dummy particle technique for boundary treatment. The associated validation referred to 2D and 3D test cases, which involved violent hydrodynamic impacts on rigid bodies.

Another interesting CFD method for the analysis of the fluid–structure interaction problems is the finite element method (PFEM). The key feature of the PFEM is the use of a Lagrangian description to model the motion of nodes (particles) in both the fluid and the structure domains. Nodes are thus viewed as particles, which can freely move and even separate from the main analysis domain representing, for instance, the effect of water droplets (Idelsohn et al., 2004). A mesh connects the nodes defining the discretized domain where the governing equations, expressed in an integral form, are solved as in the standard FEM (Onate et al., 2004). This method preserves all the classical advantages of the Finite Element Method (FEM) for the evaluation of the integrals of the unknown functions and their derivatives, including the facilities to impose the boundary conditions and the use of symmetric Galerkin approximations, combined with the flexibility of particle methods. In particular, Onate et al. (2011) developed a solution for the equations of an incompressible continuum using PFEM allowing the use of low order elements with equal order interpolation for all the variables. The proposed approach was applied to several fluid–soil–structure interaction problems involving large motion of solid–solid interfaces and bed erosion, among other complex phenomena. Onate et al. (2014) proposed a method based on PFEM and a stabilized Lagrangian mixed velocity–pressure formulation for modelling the motion of small and large particles that are submerged in the fluid. Zhang et al. (2015) revised the classical PFEM approach of Onate et al. (2004) for rigid bodies sliding process, such as landslide problems. This approach attempts to solve the complete nonlinear dynamic governing equations in the framework of solid mechanics, via a standard finite element procedure and it was validated on a real-world landslide that occurred in Southern China. Zhu and Scott (2014) extended the OpenSees software (McKenna et al., 2000) to incorporate fluid–structure interaction handling additional pressure and pressure gradient unknowns at the element level. Gimenez and González (2015) proposed a variant formulation of classical PFEM, called PFEM-2, to solve free-surface flows with pressure gradient discontinuities, based on a continuous enriched space for pressure while keeping the advantage of the possibility to use large time-steps. Finally, it is relevant to cite the theoretical and experimental work of Xia et al. (2011a), Shu et al. (2011) and Teo et al. (2012) to formulate, validate and successively integrate in a 2D hydraulic model (Xia et al., 2011b), a simple formulation for the stability threshold of flooded vehicles.

Recently, the authors of the present paper developed a 3D SPH model for body transport in free surface flows (Amicarelli et al.,

2015), which was applied here to complex 3D configurations with multiple bodies. This model adopts SPH formalism to implement the Euler–Newton equations that govern body dynamics, coupled with a WC-SPH model, which is based on a semi-analytic approach (Di Monaco et al., 2011). This involves the fluid–body interaction terms which rely on the boundary technique introduced by Adami et al. (2012), adapted for free-slip conditions, and the solid–solid interaction term of Monaghan (2005) adapted to represent a (fully elastic) impingement force. In this study, the numerical model described in Amicarelli et al. (2015) was tested in a sequence of laboratory experiments, carried out in the Hydraulics Laboratory of Basilicata University in Italy. The experiments schematized, in scale, an idealized event of a small dam failure that involved an urban floodplain with buildings and vehicles. This validation case was devoted to providing a data set for studying the flow characteristics and floating body transport phenomena in urban-like environments, and the capabilities of numerical models to accurately reproduce them.

In this paper, the agreement between numerical and experimental results, in terms of water depth, time evolution and time history of the bodies' movements, showed that the model described in Section 2 can be used instead of experimental measurements for reproducing highly dynamical shallow water problems, such as movement of large floating bodies in urban flooding events. This model was utilized in the present research as an alternative and valuable tool to investigate the behaviour of new potential mitigation structures before they are put into operational service. In particular, the hydraulic functionality of small barriers, such as beach groynes, was evaluated using the numerical model in order to propose a structural mitigation action that could be utilized to avoid solid body transport and therefore, mitigate the risk of flood damage. Following this introduction (Section 1), Section 2 provides an overview of the main features of the numerical model. Section 3 describes the validation via laboratory experiments and Section 4 describes the use of the numerical model to evaluate the hydraulic functionality of the proposed structural mitigation action. Section 5 provides the overall conclusions of the study and future work.

2. The SPH numerical model

This section describes the main features of the numerical model that was used in this study: the balance equations for fluid (Section 2.1) and body (Section 2.2) dynamics, followed by the 2-way interaction terms related to both fluid–body (Section 2.3) and solid–solid (Section 2.4) interactions. Smoothed Particle Hydrodynamics is a particle technique (each particle is considered as a computational node), based on an interpolation approach over the values of the surrounding ("neighbour") particles. The key idea is to consider that the value of the generic flow variable (f) around a generic computational particle (located at the position x_0), is approximated using convolution integrals over a limited space (the kernel support V_h is a sphere of radius 2 h, h being the kernel support size) and weighted by an analytical smoothing function (or kernel: W):

$$\langle f \rangle_{I,\underline{x}_0} = \int_{V_h} f\, W\, dx^3 \tag{1}$$

Hereafter, the under-bar symbol denotes a vector and the integral SPH approximation $\langle\ \rangle_I$ denotes the SPH approximation in the continuum of a generic function (f).

Applying the same operator to a generic derivative, computed along the spatial component x_i, and integrating by parts, the integral SPH approximation provides the following equation (after integration by parts):

$$\left\langle \frac{\partial f}{\partial x_i} \right\rangle_{I,\underline{x}_0} = \int_{V_h} W \frac{\partial f}{\partial x_i} dx^3 = \int_{A_h} f W n_i dx^2 - \int_{V_h} f \frac{\partial W}{\partial x_i} dx^3 \tag{2}$$

where n is the unity vector, locally normal to the boundary.

The volume integral in Eq. (2) is performed over the "neighbouring particles" around the computational particle. On the other hand, the surface integral should be computed over the boundary A_h of the kernel support.

2.1. SPH approximation of the balance equations of fluid dynamics

The numerical scheme for the main flow is based on a semi-analytic approach for boundary treatment. Its basic features are described in depth in the description of the semi-analytic model for main flow in Di Monaco et al. (2011). We first refer to the continuity equation for inertial flow:

$$\frac{d\rho_0}{dt} = \sum_b \rho_b (u_{b,j} - u_{0,j}) \left.\frac{\partial W}{\partial x_j}\right|_b \omega_b + 2\rho_0 \int_{V'_h} [(\underline{u}_w - \underline{u}_0)\cdot \underline{n}] n_j \frac{\partial W}{\partial x_j} dx^3 + \underline{C}_s \tag{3}$$

where ρ is density, $\underline{u}$ is the velocity vector, W is the kernel function, ω is the particle volume, and $\underline{n}$ is the vector normal to the fluid domain boundary. The summation in Eq. (3) will consider the neighbouring particles ("$_b$") around the computational particle "$_0$". Einstein's notation applies for the subscript "$_j$". The integral is instead computed over the complement V_h' (to the spherical kernel support) of the truncated kernel support where the subscript "$_w$" refers to the frontier. Finally $\underline{C}_s$ represents the coupling term for fluid–body interactions, described in Section 2.3.

On the other hand the momentum (Euler) equation is assumed:

$$\begin{aligned} \left\langle \frac{du_i}{dt} \right\rangle_0 &= -\delta_{i3} g + \sum_b \left(\frac{p_b}{\rho_b^2} + \frac{p_0}{\rho_0^2} \right) \left.\frac{\partial W}{\partial x_i}\right|_b m_b + 2\frac{p_0}{\rho_0} \int_{V'_h} \frac{\partial W}{\partial x_i} dx^3 \\ &- \upsilon_M \sum_b \frac{m_b}{\rho_0 r_{0b}^2} (\underline{u}_b - \underline{u}_0)\cdot(\underline{x}_b - \underline{x}_0) \left.\frac{\partial W}{\partial x_i}\right|_b - 2\upsilon_M (\underline{u}_w - \underline{u}_0) \\ &\cdot \int_{V'_h} \frac{1}{r_{0b}^2} (\underline{x} - \underline{x}_0) \frac{\partial W}{\partial x_i} dx^3 + \underline{a}_s \end{aligned} \tag{4}$$

where δ_{ij} is Kronecker's delta, p is pressure, g is the acceleration due to gravity, υ_M is the artificial viscosity (Monaghan, 2005), m is the particle mass and $\underline{r}$ is the relative distance between each pair of interacting particles. $\underline{a}_s$ represents the coupling term for fluid–body interactions, described in Section 2.3. A linearized barotropic state equation completes the model:

$$p \cong c_{ref}^2 (\rho - \rho_{ref}) \tag{5}$$

2.2. Modelling the balance equations for rigid body transport

The body dynamics is ruled by the Euler–Newton equations:

$$\frac{d\underline{u}_{CM}}{dt} = \frac{\underline{F}_{TOT}}{m_B}, \quad \frac{d\underline{x}_{CM}}{dt} = \underline{u}_{CM} \tag{6}$$

$$\frac{d\underline{\beta}_B}{dt} = \underline{\underline{I}}_C^{-1} \left[\underline{M}_{TOT} - \underline{\beta}_B \times \left(\underline{\underline{I}}_C\ \underline{\beta}_B \right) \right], \quad \frac{d\underline{\alpha}}{dt} = \underline{\beta}_B \tag{7}$$

where $\underline{F}_{TOT}$ is the global force acting on the solid. $\underline{\beta}_B$ denotes the angular velocity of the specific body, $\underline{\alpha}$ is the vector of the angles lying between the body axis and the global reference system. $\underline{M}_{TOT}$ represents the global moment acting on the body and $\underline{\underline{I}}_C$ the matrix of the body moment of inertia. The subscript "$_{CM}$" refers to the body centre of mass.

The global force was modelled as described in the following equation:

$$\underline{F}_{TOT} = \underline{G} + \underline{P}_f + \underline{T}_f + \underline{P}_s + \underline{T}_s, \quad \underline{T}_f + \underline{T}_s \cong 0 \tag{8}$$

$\underline{G}$ represents the gravity force, while $\underline{P}_f$ and $\underline{T}_f$ represent the sum of the pressure and shear forces provided by the fluid. Analogously $\underline{P}_s$ and $\underline{T}_s$ are the sum of the normal and the shear forces provided by other bodies or boundaries (solid–solid interactions). As this study focused on inertial and quasi-inertial fluid flows, turbulence scheme and tangential stresses (simplifying hypothesis) were not implemented. Future research is needed to extend the formulation of Section 1 to a wider category of fluid flows.

In the Euler–Newton equations, the fluid–solid interaction is expressed by the following pressure force:

$$\underline{P}_f = \sum_s p_s A_s \underline{n}_s \tag{9}$$

The computational body is numerically represented by solid volume elements, here called (solid) body particles ("$_s$"). Some of them describe the body surface and are referred to as "surface body particles". These particular elements are also characterized by an area and a vector $\underline{n}$ of norm 1 perpendicular to the body face (the particle belongs to) and points outward to the fluid domain (inward to the solid body). The body particle pressure is computed as described in Section 2.3. Finally, the global moment is discretized as follows:

$$\underline{M}_{TOT} = \sum_s \underline{r}_s \times \underline{F}_s \tag{10}$$

While the body particle velocity is the vector sum of the body velocity and the relative velocity of the particle, with respect to the body centre of mass ($\underline{r}_s \equiv \underline{r}_{s,CM}$):

$$\underline{u}_s = \underline{u}_{CM} + \underline{\beta}_B \times \underline{r}_s \tag{11}$$

The body particle normal and position need to be updated at every time step:

$$\underline{n}_s(t+dt) = \underline{\underline{R}}_B \underline{n}_s(t), \underline{x}_s(t+dt) = \underline{x}_{CM}(t+dt) + \underline{\underline{R}}_B \underline{r}_s \tag{12}$$

according to the rotation matrix of the body R_{ij}, which in turn depends on the body orientation:

$$d\underline{\alpha}_B = \underline{\beta}_B dt \tag{13}$$

2.3. Modelling the fluid–body interaction terms

The fluid–body interaction terms rely on the boundary technique introduced by Adami et al. (2012), here adapted for free-slip conditions. The fluid–body interaction term in the continuity equation Eq. (9), can be formulated as follows:

$$\underline{C}_s = 2\rho_0 \sum_s [(\underline{u}_s - \underline{u}_0) \cdot \underline{n}_s] W'_s \omega_s \tag{14}$$

and the analogous term in the momentum equation is written as

$$\underline{a}_s = \sum_s \left(\frac{p_s + p_0}{\rho_0^2} \right) W'_s m_s \tag{15}$$

The pressure value of a generic neighbouring (surface) body particle "$_s$" can be derived by:

$$p_s = \frac{\sum_0 \left[p_0 + \rho_0 (\underline{g} - \underline{a}_s) \cdot (\underline{r}_{s0} \cdot \underline{n}_s) \right] W_{0s} \left(\frac{m_0}{\rho_0} \right)}{\sum_0 W_{0s} \left(\frac{m_0}{\rho_0} \right)} \tag{16}$$

where each fluid particle–body particle interaction is represented by the subscript "$_{s0}$".

It is worth mentioning that free-slip conditions represent a useful approximation in this model. It is not possible to correctly model boundary layers without a multi-resolution SPH model at the high Reynolds number investigated in Section 3. In these cases, using no-slip conditions on the solid body surfaces makes the viscous friction as well as the hydrodynamics forces on the floating objects to be widely overestimated.

2.4. Modelling the solid–solid interaction terms

SPH modelling of impacts between solid structures have been reported in several studies. Among them, a relevant application field is represented by birdstrikes, i.e. impacts between an aircraft and foreign objects (e.g. birds). Several studies on this topic provide major references to represent impacts of solid bodies. McCarthy et al. (2004) coupled the Finite Element (FE) method with SPH to simulate the impact of a bird with the leading edge skin of an aircraft (both made of SPH particles). Grimaldi et al. (2013) presented a parametric study on birdstrikes by focusing on the windshield absorption of the impact energy. Analogous SPH numerical schemes can be adopted in SPH modelling for the transport of solid bodies in free surface flows (Monaghan, 2005). In particular, Amicarelli et al. (2015) provided some preliminary validations for its numerical treatment of the impacts between solid bodies.

The solid–solid interaction term in Eq. (8) represents a (full elastic) impingement force.

For a body–body interaction it can be expressed as follows:

$$\underline{P}_s = -\alpha_I \sum_j \sum_k \frac{2u_{\perp jk}^2}{r_{per,jk}} \frac{m_j m_k}{m_j + m_k} \Gamma_{jk} \left(1 - \frac{r_{par,jk}}{dx_s} \right) \underline{n}_k \tag{17}$$

This force involves interactions between all the body particles "$_j$" of the computational body "$_B$" and their corresponding neighbour body particles "$_k$", belonging to the neighbouring body. The direction of a generic partial force, related to each particle–particle interaction, is aligned with the normal of the neighbour particle. Its magnitude depends on particle masses, the relative position of the interacting particles, the impact velocity $u_\perp$ and the normalizing factor α_I.

r_{par} and r_{per} are parallel and the perpendicular components of the relative distance between the two interacting particles, respectively (see Fig. 1). The term within brackets in Eq. (17) deforms the kernel support of the body particles "$_j$", so that it only develops aligned with the normal of the neighbouring particle (dx_s represents the size of the body particles). Γ is a further weighting function, different from W. The impact velocity is computed as the maximum value of the relative velocity (projected over the normal of the neighbouring particle), estimated over all the body particle interactions during the whole duration of the approaching phase ($t_0 \leqslant t \leqslant t_a$) of the impingement:

$$u_{\perp jk} = \max_{j,k,t} \left\{ \left| \left[(\underline{u}_j - \underline{u}_k) \cdot \underline{n}_k \right] \right| \right\}, \quad t_0 \leqslant t \leqslant t_a \tag{18}$$

α_I is a normalizing parameter which allows for the treatment of whole solid bodies, instead of particle–particle impingements:

$$\alpha_I = \sum_K \frac{1}{r_{per,BK}} \frac{m_B m_K}{m_B + m_K} \Gamma_{BK} \Bigg/ \sum_j \sum_k \left[\frac{1}{r_{per,jk}} \frac{m_j m_k}{m_j + m_k} \Gamma_{jk} \left(1 - \frac{r_{par,jk}}{dx_s} \right) \right] \tag{19}$$

with the subscript "$_K$" denoting a generic neighbouring body.

On the other hand, it is necessary to model body–boundary interactions. In this frame the boundary is considered as a body with infinite mass and discretization tending to zero (the semi-analytic approach that is used to model fixed frontiers is in fact an integral method). The interaction force then becomes:

$$\underline{P}_s = -\alpha_I \sum_j \sum_k \frac{2u_{\perp jk}^2}{r_{per,jk}} m_j \Gamma_{jk} \underline{n}_k, \quad \alpha_I = \frac{m_B}{r_{per,Bk}} \Gamma_{Bk} \Bigg/ \sum_j \sum_k \left[\frac{m_j}{r_{per,jk}} \Gamma_{jk} \right] \tag{20}$$

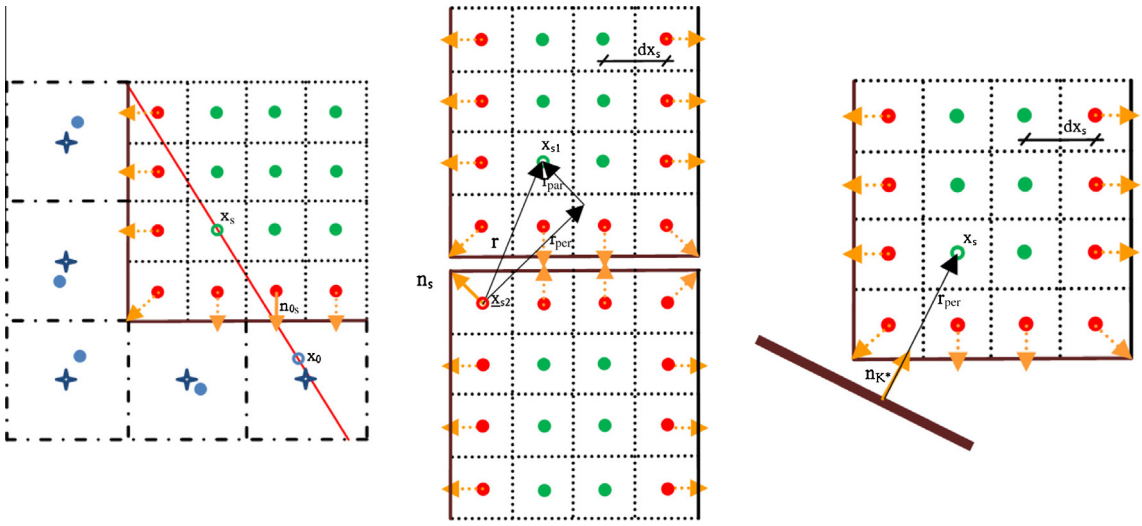

Fig. 1. Schematic representations of 2D non-homogeneous SPH interactions. Left panel: detection of the normal $\underline{n}_{0s} = \underline{n}_s$ in the interaction of a generic inner body particle ($\underline{x}_s$) with a generic fluid particle ($\underline{x}_0$); red circles: barycentres of surface body particles; green circles: barycentres of the inner body particles; blue circles: numerical position of the fluid particles; blue crosses: barycentres of the fluid particles; dashed lines delimit the volume (surface in 2D) of the numerical elements; orange arrows: normal vectors of the surface body particles; continuous lines: body boundary. Centre panel: estimation of r, $\underline{r}$ and $\underline{r}_{per}$, $\underline{r}_{par}$ in the interaction between a generic inner body particle ($\underline{x}_{s1}$) and a generic surface body particle ($\underline{x}_{s2}$). Right panel: interaction of a generic inner body particle ($\underline{x}_s$) with a frontier "k"(brown thick line). (For interpretation of the references to colour in this figure legend, the reader is referred to the web version of this article). *Source:* Amicarelli et al. (2015).

with the subscript "$_k$" here denoting a neighbouring frontier (see Fig. 1).

3. Validation via laboratory experiments

Flash-floods are defined as sudden events with high peak discharges, produced by severe thunderstorms that are generally limited in areal extent (Lucìa et al., 2015). Flash floods can also result from dam-breaks, or even from ice jams on a river or stream during the winter months. The SPH model described in the previous chapter was validated on a 3D experimental dam break event that was characterized by its rapidity, the small area of interest and where the flow can be considered as inertial. Dam break events represent a typical application field in SPH modelling. Among others, Colagrossi and Landrini (2003) defined a 2-phase (gas–liquid) SPH model to represent dam break phenomena. Crespo et al. (2008) highlighted the differences in modelling dam breaks over wet and dry beds by using Weakly-Compressible SPH models.

Recently, Razavitoosi et al. (2014) presented a 2-phase (solid–liquid) SPH model, which simulates the propagation of 2D dam break waves over mobile beds. Džebo et al. (2014) implemented a SPH model, whose boundary treatment imposes free-slip conditions with friction: validations were provided for a dam break on a complex 3D topography by comparisons to both measures and Finite Volume numerical results. Finally, Aureli et al. (2015) showed a relevant model inter-comparison between SPH and mesh-based techniques (both 3D and 2D) on a typical dam break event with a squat obstacle.

The proposed experimental configuration, described in detail in Section 3.1 was more complex than other experimental configurations available in the literature (e.g. Gómez-Gesteira and Dalrymple, 2004; Soares-Frazão and Zech, 2007) because it involved the transport of floating bodies and their interactions with two fixed obstacles, a mobile gate (representing a dam) and a down-flow wall. This configuration was reproduced on a 1:1 scale in the numerical model (Section 3.2) and, finally numerical results were validated, in terms of flow depth and time history of the bodies' movements, through a qualitative and quantitative comparison to experimental data (Section 3.3).

3.1. Experimental set-up

The experimental tests were carried out on a tilting flume with a rectangular cross-section of 0.5 m in width and 0.5 m in height (Fig. 2a) in the Hydraulics Laboratory of Basilicata University, Italy. The main structure of the flume consisted of steel parts, while the lateral walls were made of transparent glass and the floor of the channel of bakelite (Mirauda et al., 2011) (Fig. 2a). The dimensions of the experimental setup were $2.500 \times 0.500 \times 0.500\ m^3$, while the obstacles each measured $0.300 \times 0.150 \times 0.300\ m^3$. The first obstacle (Obstacle 1) was placed at a distance of 1.40 m from the left boundary of the reservoir and 0.020 m away from the top edge, while Obstacle 2 was

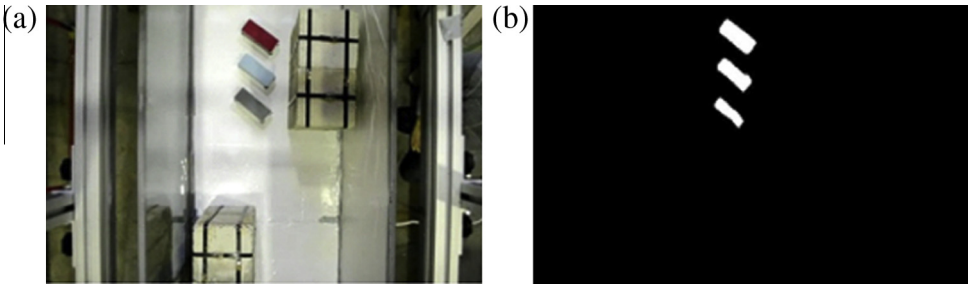

Fig. 2. (a) Original video frame; (b) blob image of extracted/detected objects.

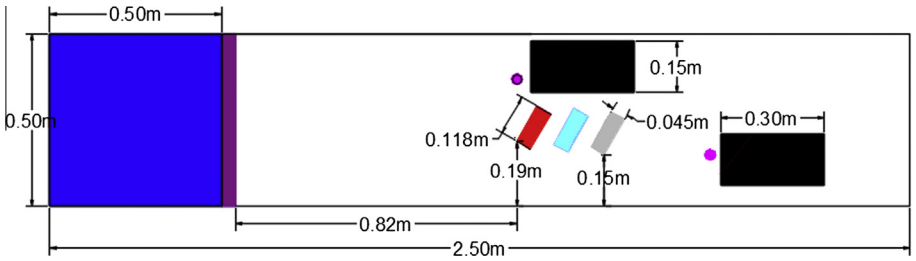

Fig. 3. Numerical and experimental domain.

placed at a distance of 1.950 m from the left boundary and 0.060 m away from the bottom edge.

The three transported bodies were parallelepipeds with dimensions of $0.118 \times 0.045 \times 0.043$ m, masses of $m_B = 0.025$ kg, and density of $\rho_s = 111$ kg/m^3. The position of the vehicles was evaluated on the basis of the steering kinematics equation for vehicles, (Pacejka, 2005), in order to represent a typical parking space designed according to the steering kinematics of vehicles upon their entry and exit from parking, the optimal angle orientation of the vehicles, and other good practices in parking space design.

The three bodies were initially at rest, with their centres of mass located at 1.407 m, 1.515 m, and 1.622 m away from the left boundary of the reservoir, respectively at 0.229 m, 0.221 m, and 0.213 m from the right wall, and at 0.0215 m from the bottom on which they rested. The flow inside the channel was estimated through measuring the water depth evolution over time using two resistive gauges located upstream of the fixed obstacles that recorded the flow depth value with a frequency of 25 Hz. The points where the flow depth was measured are indicated in magenta in Fig. 3.

The bodies' displacements were evaluated by an image analysis through two Charge Coupled Device cameras (CCD) located at different points, recording lateral and plan views of the experiment, owing to a stainless steel modular system fixed to the channel structure. The space recorded by the cameras was limited to a portion of the channel from 1.4 m to 2.1 m from the left side of the experimental setup.

The time history of the bodies' movements was provided using an image analysis method that combines two algorithms: the object extractor (Fig. 2b), and the object tracker of the "Matlab" image processing library. The first algorithm, i.e. the object extractor, was utilized to detect the bodies by extracting the information related to them from the whole recorded image using the thresholding technique of Gonzalez and Woods (2008). Once the objects were detected, the second algorithm, i.e. the object tracker, was utilized to recognize the position of the objects in time on each image.

When the position of an object could not be evaluated, e.g. the object was not sufficiently visible in the image because it was covered by the water flow or by the fixed obstacle, a Kalman Filter (Simon, 2006) was used. The Kalman Filter class of "Matlab" was used for the prediction of the new position of the object via the last known states (position, velocity). The experiment was repeated several times (A, B, C, D and E), each of which showed similar results, confirming the reliability of the tests and of the collected data. In particular, the collected experimental data of water depth was averaged before comparison with the numerical model to obtain a summary index of efficiency of the numerical model reproduction of flow water. The time evolution experimental data of the floating bodies' displacement were compared in a lumped way, i.e. all the experimental measures were utilized for the comparison, in order to evaluate the numerical model performance while taking into account the potential uncertainties in the experimental simulation with an "ensemble" approach.

3.2. Numerical model simulation set-up

The numerical implemented geometry reproduced the experimental apparatus, ($2.500 \times 0.500 \times 0.500$ m^3), at a scale of 1:1; both of these represented a reproduction, at a scale of 1:40, of the failure of a big tank or a small dam involving a link road with buildings (fixed obstacles) and vehicles (floating bodies) in the immediate vicinity of the water reservoir. The evolution of a dam break front was produced through a regular (non-instantaneous) lifting of a gate, which initially contained the (initially inertial) water reservoir of dimensions ($0.100 \times 0.500 \times 0.500$ m^3), as seen in Fig. 3.

In the laboratory experiments, an automatic mechanism opened the gate very quickly in order to simulate, as closely as possible, a dam-break event. In the numerical model, the height of the gate was shortened, i.e. the upper part that was not involved in the simulation was cut, compared to the gate of the experiment in order to reduce the computational time of the numerical simulation. This did not affect the final results because the water in the reservoir did not overpass the gate, which was modelled as a numerical body and not a frontier with the imposed kinematics, meaning that its influence on the fluid domain fields was estimated according to the formulations described in Section 2.3. The gate began to lift at $t = t_0 = 0.00$ s with a uniform vertical velocity of $w = 0.11$ m/s until $t = 2.00$ s, when the lifting stopped. The maximum value of the numerical acceleration was around 2–5 g, which remained under the imposed threshold to avoid providing an unreliable estimation of the body particle pressure (10 g). We set $dx/dxs = 2$, with $dx = 0.008$ m to represent the size of the fluid particles and dxs to represent the size of the body particles, respectively. The estimated parameters were normalized assuming the velocity scale as $\sqrt{2gH} = 1.96$ s where $H = 0.1$ m.

The numerical simulation (Fig. 4a) represents a wave front that overcomes a link road in the immediate vicinity of the water reservoir. The model includes two fixed structures (buildings) as well as three floating bodies (vehicles) that finally impact at a down-flow wall.

3.3. Analysis of the numerical simulation and verification through a comparison with experimental data

Fig. 4 reports the absolute value filed time sequence of the normalized velocity in plan view simulated with the numerical model described in Section 2. As Fig. 4b shows, the water front struck the first fixed obstacle and partially reversed its flow, moving away from the obstacle's upstream face. At the same time ($t = 1.00$ s), the water front began transporting the first body (Body 1) downstream (Figs. 4a and 5a), before striking the other bodies as well. The third body (Body 3), which was positioned farthest from the gate, was the first to impact ($t = 1.40$ s) the down-flow obstacle (Obstacle 2) and was subsequently deviated laterally (Figs. 4c and 5c) after being lifted into the air due to the impact.

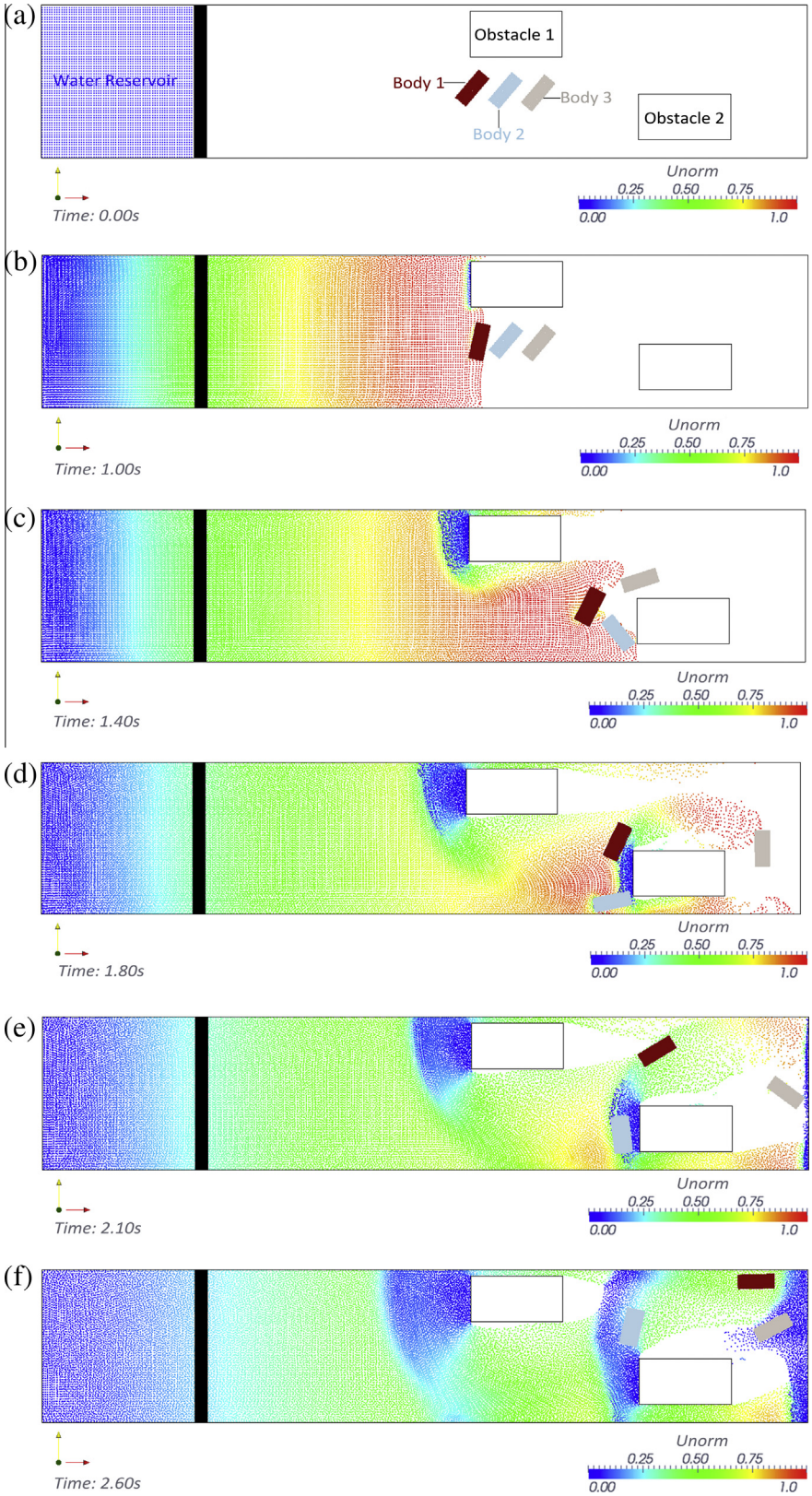

Fig. 4. Dam break with bodies transport. Time sequence of the field of the absolute value of the normalized velocity – "Unorm" (plan view).

Subsequently, the other bodies also struck Obstacle 2, were lifted up into the air, and then fell into the water and remained on the up-stream side of Obstacle 2. At around $t = 1.80$ s Body 1 began to overpass the upwind face of Obstacle 2 while Body 3 remained at the edge of the system boundary (Fig. 4d). Body 2 remained upstream of Obstacle 2 (Fig. 5d) until $t = 2.6$ s, at which point it began to bypass the obstacle (Fig. 4e). Finally, the water front and the surface wave were reflected by the down-flow boundary

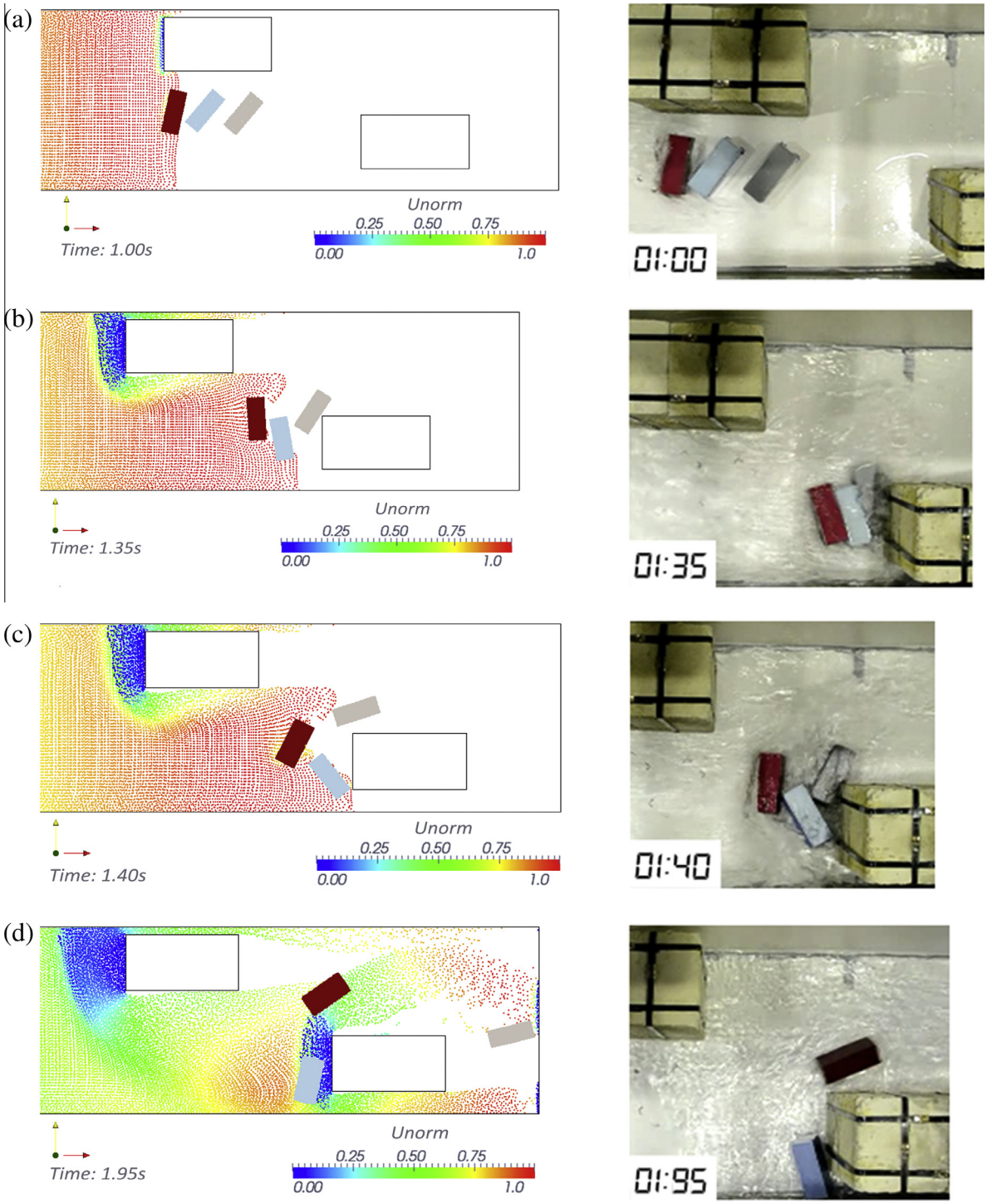

Fig. 5. Dam break with bodies transport. Graphical comparisons of the body trajectory. Left: SPH model. Right: experiment.

and slowly transported the bodies back upstream (Fig. 4f). During the time evolution of the simulation, cavity zones were evident that were not rapidly filled by the water mass or surface wave of the water flow due to the rough resolution.

The main disadvantage of the SPH method is its high cost with regard to computational time. SPH models give more accurate results using a larger number of particles, which strongly increases the computational cost of simulations, as a search for all neighbouring particles must be performed at each time step. This is especially true in 3D applications when realistic cases are simulated. For the N-body algorithm, usually, the computational power required grows as the square on the particle number N. Moreover, in this paper, we notice that due to the chaotic features of the phenomenon (i.e. highly non-linear phenomenon), which is still dependent on the SPH spatial resolution, the accuracy increase requires an expensive computational cost that could be unbalanced or prohibitive with standard desktop hardware. In particular, in this simulation we used a particle resolution of 46,128 on an Intel Xeon CPU E5-2643 3.3 GHz and 8 GB RAM resulting in a total elapsed time equal to 3 d 9 h 47 m 19 s. During the tuning of the model, the chosen resolution assumes a good trade-off between quality of results and CPU cost. In this context, new

technological and methodological approaches could reduce this shortcoming. On one hand, the SPH model could take advantage of the relatively recent capability offered by dedicated Graphic Cards (Graphic Processing unit – GPU), which can be used to perform High Performance Computing on classical personal computers rather than traditional clusters of CPUs (Viccione et al., 2008). A particular feature of these operations is that the same instructions (e.g. matrix multiplications) can be performed in parallel over different data to accelerate numerical simulations (Brodtkorb et al., 2013). In this way, the numerical scheme ensures a robust treatment of wet-dry fronts and allows for accurate simulation of flooding (Vacondio et al., 2014). On the other hand, low quality resolution of this simulation at shallow water depths should be addressed by the adoption of a new methodological approach for the wet-dry interface, such as in Vacondio et al. (2012), where a particle splitting procedure was introduced into a classical SPH model in order to conserve mass and momentum by varying the smoothing length, velocity and acceleration of each refined particle.

In spite of the above shortcomings, as shown in the graphical comparison between the numerical and experimental model in Fig. 5, the model adequately reproduced the main features of the body trajectories. Nevertheless, the numerical trajectories could not accurately reproduce the impact of body 3 on the second fixed obstacle (Fig. 6e), nor could they anticipate the exit of body 1 from the recirculation zone in the upstream zone of obstacle 2 (Fig. 6a). However, in the numerical model, the overestimation or underestimation of the position of the bodies near the zone of impact to the fixed obstacle was caused by the limitations of the image detection process to precisely estimate the centre of mass when the orientations of the bodies were rapidly changing in the video frame and water flows partially covered the objects. On the other hand, as shown in the quantitative comparison of Fig. 6, the vertical positions of the bodies were accurately predicted, even when body 2 impacted against the second obstacle, was lifted up with the rising water front and then fell down.

The relative percentage errors for the values of the x-coordinate of the centre of mass of the body (Fig. 6a, c and e), considering only the interval of time when the bodies were in motion, were less than 5% for most ranges of the data (i.e. for 72% of the data points for body 1, 83% of the data points for body 2, and 48% of the data points for body 3). The highest relative percentage error was less than 15%.

The numerical predictions for the z-coordinates of the centre of mass of the body, (Figs. 6b, 7d and 6f) were less precise than the x-coordinate predictions. However, the relative percentage errors were less than 10% for almost 50% of the data, and were above 20% for only 10% of the data. Moreover, in order to value in a more clear way the forces acting on the bodies, the Finite Difference Method (FDM) was used to calculate the instantaneous velocity and acceleration of the floating bodies, starting with the measured displacements. A centred finite difference scheme with error of order $O(h^4)$ (Mirauda et al., 2013), was used for both the first and the second derivative of displacements in directions:

$$\dot{x}_{i=x_{t_i}} = \frac{x_{i-2} - 8x_{i-1} + 8x_{i+1} - x_{i+2}}{12\Delta t} + \frac{1}{30}x_{ttttt}(\xi)\Delta t^4$$
$$\ddot{x}_{i=x_{tt_i}} = \frac{-x_{i-2} + 16x_{i-1} - 30x_i + 16x_{i+1} - x_{i+2}}{12\Delta t^2} + \frac{1}{90}x_{tttttt}(\xi)\Delta t^4 \quad (21)$$

where Δt is the sampling time or the inverse of the acquisition frequency of signals.

The forces acting on a flooded vehicle could be considered similar to those acting on a coarse sediment particle (such as gravel or cobble) resting on the bed of a river. As the experiments can represent floodwater flows around a vehicle parked on a road, the flow usually exerts three forces on the vehicle, including a lift force (F_L), a drag force (F_D) and a buoyancy force (F_B). It is assumed that the wheels of a vehicle are all locked against any movement as it is parked on a road, thus a frictional force (F_R) will be produced to resist the vehicle from sliding on the road surface. For real cars the friction angle tires/asphalt can be up to 100%. In accordance with Xia et al. (2011a,b), we can hypothesize that the total force acting on the flooded vehicle is controlled by the above four forces plus the gravitational force. Moreover, most of the existing literature regarding a car's hazard is related to a balance between hydrodynamic forces and friction. In the first part of the experiment, described in this paper, until the impact of the floating bodies against the fixed obstacle, the principal forces, along the x direction, involved in the transport of the bodies are the hydrodynamic and friction forces assuming that the fluid flow is inertial or quasi-inertial, the channels are dry and the bodies are not submerged or partially submerged by the flow. Instead, when the floating bodies impact against the fixed obstacle, there is a very rapid decrease in the velocity of the bodies (also to negative values) due to the pressure of the fixed obstacle and, hence, the latter plays the main role in the balance of the forces acting on the bodies. In the final part of the experiment, the buoyancy force also plays a significant role limiting the role of sliding processes. Hence, in the first part of the experiment, the total force acting on the floating bodies can be approximated as the difference between hydrodynamic and friction forces:

$$F_D - F_R = ma \quad (22)$$

where a is the acceleration and m the mass of the body.

The maximum value of the acceleration for the three bodies was around 2–4 g in this part of the experiment. Due to the contact surface material used, such as Bakelite, the friction angle between the bodies and the channel in the experiment was approximately 20°; thus, the friction coefficient was 0.36 (Cox and Ball, 2001; Keller and Mitsch, 1993). Therefore, the friction is less than 15% of the flow force:

$$F_R/F_d = F_R/(ma + F_R) \quad (23)$$

and, hence, we can consider that it does not play an important role in this experiment. This is in accordance with the simplifying hypothesis of the numerical model (see Eq. (8)) that did not implement tangential stresses. This simplification limits the application of the model to a wider category of fluid flows. However, it does not affect the results proposed in the simulation performed in Section 4, in which a mitigation solution to avoid the transport of vehicles in the case of a dam-break event was tested, because neglecting the friction force in the numerical model, we overestimated the total force and, hence, we tested the proposed mitigation solution in excess of caution with respect to the potential real loads. Moreover, this simplification neglects the resistance at the bottom and introduces errors in the propagation of gravitational wave surfaces, which are highlighted in the following. As shown in Fig. 5, the measured flow depths were generally in good agreement with the numerical model predictions. In addition, the Nash–Sutcliffe model efficiency coefficient (Nash and Sutcliffe, 1970), used to assess the predictive power of hydrological models, was adapted to evaluate the efficiency of the numerical model:

$$\eta = 1 - \left(\sum_{i=1}^{n} (h_{ei} - h_{ni})^2 \Big/ \sum_{i=1}^{n} (h_{ei} - \bar{h}_e)^2 \right) \quad (24)$$

where h_e is the experimental value of the free surface height, $\bar{h}_e$ is the mean of all the experimental values and h_n is the value from the numerical model.

The value of the efficiency coefficient was around 0.8 for the flow depth at the up-flow face of obstacle 1 but was only 0.53 for the flow depth at the up-flow face of obstacle 2, due to higher overestimation of the flow depth by the numerical model after the

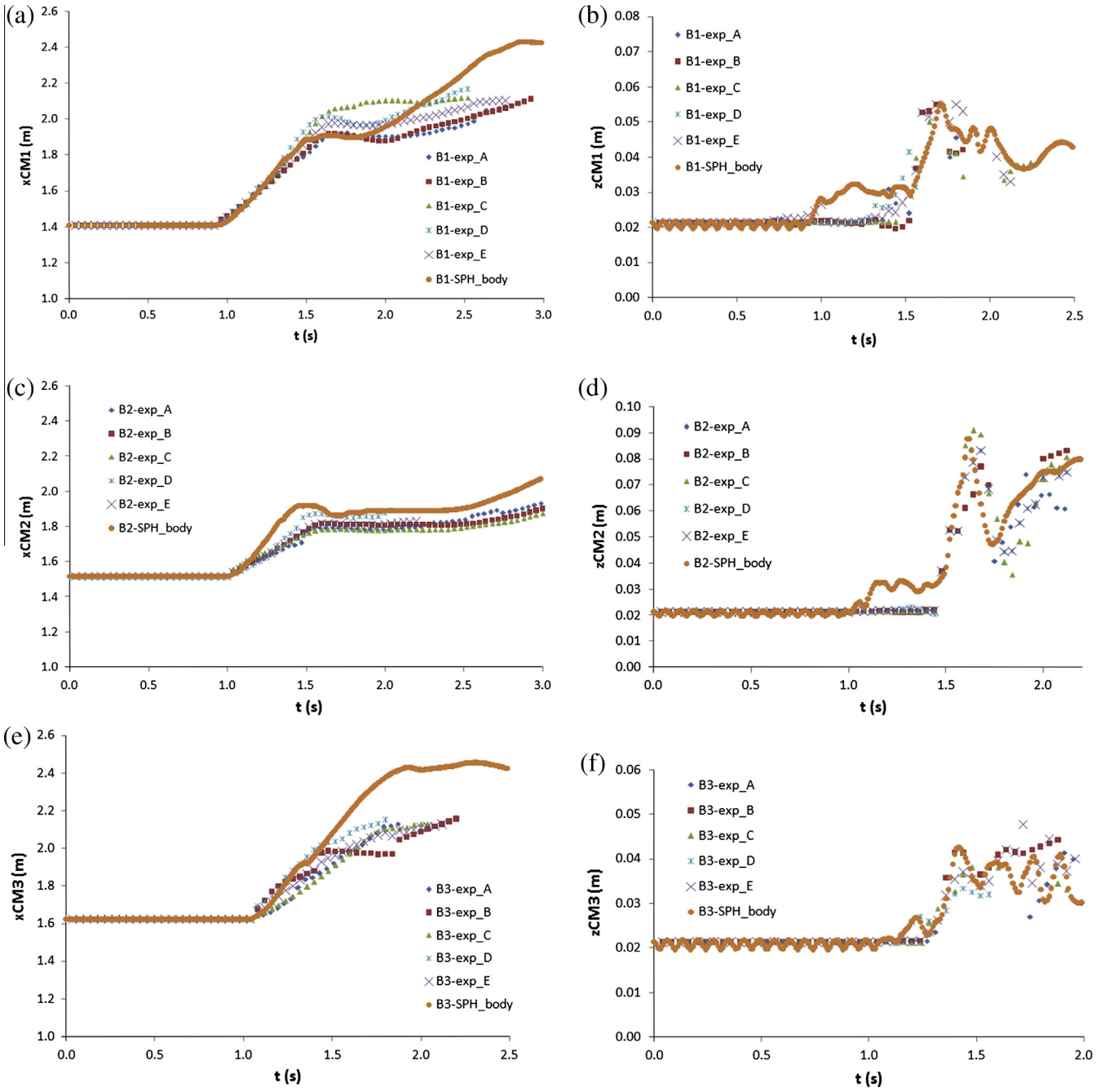

Fig. 6. Dam break with bodies transport: validations over experimental values. (a, c and e): time evolution of the *x*-coordinate of the centre of mass of the body; (b, d and f): time evolution of the *z*-coordinate of the centre of mass of the body.

peak flow, likely caused by the reflection of the front wave against the obstacles. However, the peaks themselves were accurately estimated, as can be seen in Fig. 7. In the decreasing flow height phase following the peak, an underestimation of the experimental data as opposed to the numerical results, can be noted.

In view of these generally satisfactory results, the model showed that it has reached a maturity that allowed for quantitative comparison with experimental measurements with accuracy levels similar to those observed in laboratory experiments. Hence, the numerical model, in comparison to the time intensive, expensive, and difficult to perform laboratory experiments, was used to further analyse the impacts of structural mitigation interventions. Indeed, the model shortcomings were not important enough to significantly affect the outcome of analyzing the impacts of structural mitigation interventions, described in the following section. The mitigation structures can be used to limit the water flow velocity in the channel, therefore, the accuracy error in the time evolution of the horizontal position of the bodies is accordingly limited. On the other hand, the time evolution of the vertical position of the bodies is properly estimated and, hence, this will affect the vertical efficiency of the mitigation structures.

4. Application of the SPH model to mitigate floating bodies in cases of urban flooding

Flooding phenomena are difficult to analyse (Nourani et al., 2014) and, therefore, experimental tests are necessary to validate the accuracy of numerical modelling and to demonstrate its capabilities in reproducing flooding phenomena. Hence, the SPH

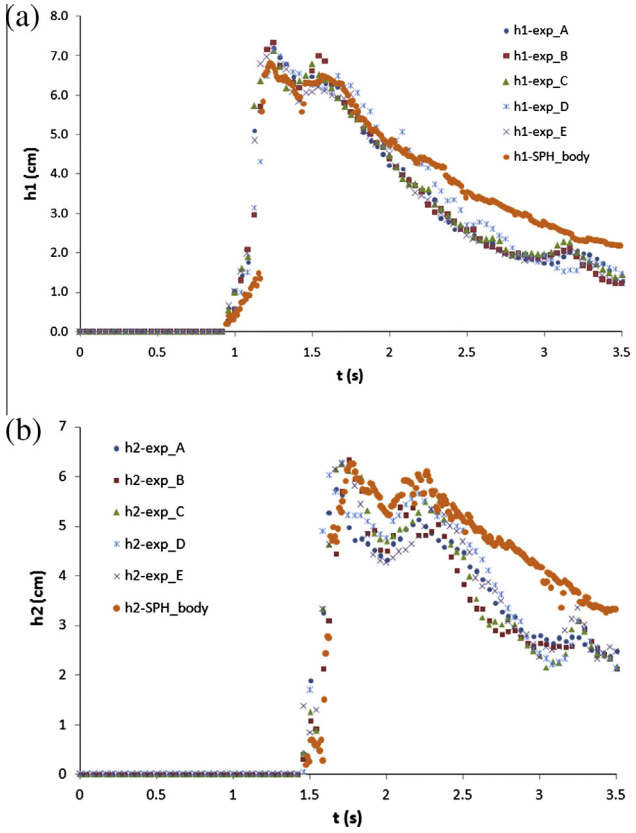

Fig. 7. Dam break with bodies transport: validations over experimental values. Time evolution of the free surface height (h1) at the up-flow faces of obstacle 1 (up-flow) and time evolution of the free surface height (h2) at the up-flow faces of the obstacle 2 (down-flow).

numerical model, following validation with experimental data, was used to investigate the hydraulic efficiency of possible structural measures as well as to contrast the floating body transport phenomena in free surface flows. The SPH numerical tools were also capable of reporting more parameters, such as velocity, pressure, free surface elevation, and the body and fluid particle trajectories, than could be measured from laboratory experiments.

Groynes (barriers) are a technical solution for certain kinds of flood events, such as sea storms, which can also be applied to flash or pluvial (rainfall-induced) urban floods where the rapidity of the event and the intensity of the flow impact are obviously less violent than that of a dam-break event. This study evaluated the usefulness of groynes to avoid the transport of vehicles in the case of a dam-break event. Groynes can be used as part of a broader approach to more sustainable water resources management; this transition to more integrated and adaptive water resources management (Halbe et al., 2013; Kolinjivadi et al., 2014; Straith et al., 2014; Inam et al., 2015) is increasingly becoming important given the myriad challenges facing water resources due to climate change (e.g. Adamowski et al., 2010; Nalley et al., 2013; Pingale et al., 2014) and many other issues.

In the geometrical configuration of the experiment described in Figs. 2a and 4, two groynes were introduced for each floating body. The first was located near the upstream face of the floating body, and the latter near the downstream face. The barriers were parallelepipeds with an elevation 1/3 less than and a length 4% larger than that of the bodies. They were modelled as fixed numerical bodies (with imposed kinematics). In the configuration, a small parallelepiped between the first buildings and the floating bodies was also introduced and modelled as a frontier that represented a sidewalk (Fig. 8a).

The gate began to lift at $t_0 = 0.00$ s, with a uniform vertical velocity $w = 0.11$ m/s until $t = 1.30$ s, when lifting stopped. When the gate was opened, the waterfront impacted the first obstacle ($t = 0.95$ s) and was deflected and backflowed to a certain extent. At the same time, the water front reached the first barrier. The water flow was confined between the barriers and the channel bottom until 1.40 s, when the water front impacted the second fixed obstacle. Subsequently, the first barrier was submerged by the water flow and the first body moved out of the confined region between the two barriers ($t = 1.45$ s). The first body then impacted the downstream barrier ($t = 1.70$ s) and bounced backward, lifting up in the air. It then fell down into the water and was transported by the vortex of the recirculation zone confined in the region between the barriers and the right wall of the channel. At around $t = 2.55$ s, the first body impacted the second fixed obstacle and was deviated laterally, while the third obstacle was freed from its two barriers and transported by the water flow towards the recirculation zone of the first fixed obstacle. Finally, at $t = 2.90$ s, as reported in Fig. 8b where the field of the normalized velocity absolute value of the flow (called "*Unorm*") is represented, the first and third bodies were slowly transported to the downstream boundary while the second body was still in the process of overcoming its downstream barrier.

As can be seen from Fig. 8b, the proposed configuration of barriers did not appear to have been effective; the bodies escaped from the barriers and flowed downstream as the flow overcame the barriers, which proved inefficient at confining the flow in the longitudinal direction. As such, a simple configuration was analyzed in order to understand the cause of this failing. The new and simpler configuration was composed of a single body protected by two barriers (see ID configuration no. 1 of Table 1). There were no buildings in the road, i.e. no fixed obstacles in the channel, but the walls of the channel could represent a group of contiguous buildings. The configuration also included two parallelepipeds between the wall and the floating body, representing sidewalks (similarly to the previous configuration). The orientation of the vehicles to flow was selected because it resulted in a higher potential critical condition: It provided a large bluff area projected normal to the flow, if comparing to the front or rear ends of the vehicle, thus, the cross sectional area of flow through vehicles was reduced. The boundary conditions were the same as the previous simulation (Fig. 8). In this case, the water front impacted the first barrier at $t = 0.90$ s. The body moved only in the zone confined between the two barriers until the water flow overcame the upstream barrier ($t = 1.45$ s), while the water front impacted the downstream end of the channel. The water flow that overcame the upstream barrier pushed the body out into the middle of the channel ($t = 2.5$ s) (Fig. 10), after which the surface waves that were reflected from the downstream end moved back upstream ($t = 3.1$ s), slowly bringing the body back up with them. In this configuration of Fig. 9, the cause of the inefficiency could be that the water flow was not confined along the longitudinal direction but it could move the object from different sources.

Therefore, in a new simulation, the groynes were positioned on both sides of the street, i.e. the lateral sides of the channel, in order to confine the water flow to the middle of the channel (see ID configuration no. 2 of Table 1). During the simulated event of Fig. 10, the bodies moved within the area confined by the groynes and were not transported to the downstream areas (Fig. 10b). In this configuration, the groynes were efficient in confining the flow along the centre of the channel, reducing the extent and intensity of the high pressure and, so, limiting the effect of the flow on the actual side ends of the vehicles that were facing flow that, as demonstrated in Teo et al. (2012), had the most prominent effect on the transport of the vehicle (Fig. 10a). Moreover, the groynes avoided the submersion of the vehicles and at the same time

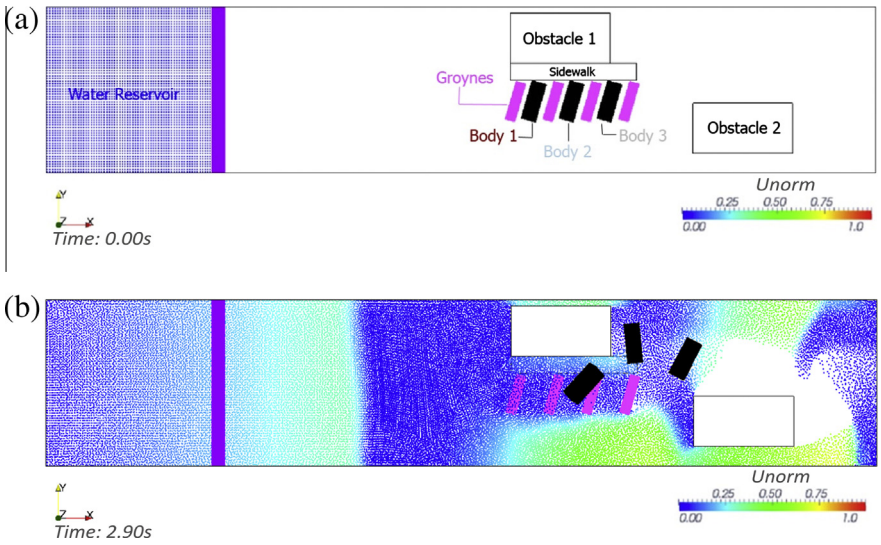

Fig. 8. Dam break with 3 bodies transport and 4 groynes. Initial (a) and final (b) time instant of the field of the normalized velocity absolute value – "Unorm" (lateral view).

Table 1
Summary table of the different configurations performed in this study to identify the most appropriate one during flash-flood events that highlights the potential hydraulic functionality of groynes.

ID configuration	Name of the configuration	Schema of the configuration	Description and outcome of the configuration
1	Dam break with one floating body held in individual spaces delimited by two groynes	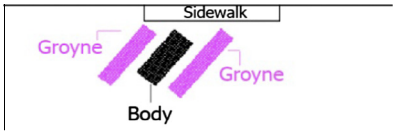	The configuration includes two magenta parallelepipeds that represent the groynes, one black parallelepiped that is the vehicle and two no brush parallelepipeds, between the wall and the floating body, representing sidewalks. The water flow can transport the vehicle to the downstream areas
2	Dam break with two floating bodies held in individual spaces delimited by four groynes	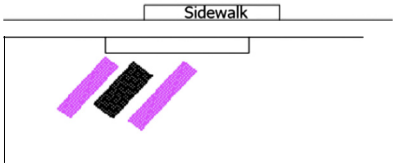	The groynes are positioned on both the sides of the street, i.e. the lateral sides of the channel. During the simulated event, the bodies moved within the area confined by the groynes and were not transported to the downstream areas
3	Dam break with four floating bodies bounded by only one upstream and one downstream barrier to each set of two bodies	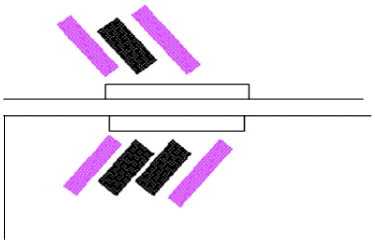	In this configuration, multiple bodies are positioned side-by-side along the same side of the road and the groynes are positioned only at the beginning and at the end of the idealized vehicle lines. The results of this simulation show that the bodies are free to move, not being confined in the space between the two barriers
4	Dam break with four floating bodies held in individual spaces delimited by groynes	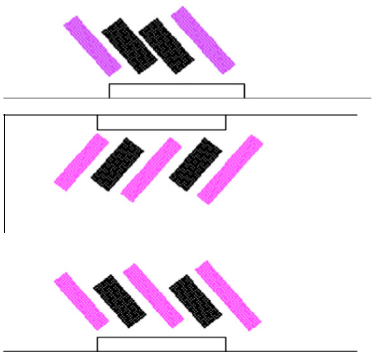	In this configuration, multiple bodies are positioned side-by-side along the same side of the road and the groynes are positioned upstream and downstream of each floating body. As in configuration no. 2, the bodies remain confined in the spaces delimited by the groynes for the entire duration of the simulation

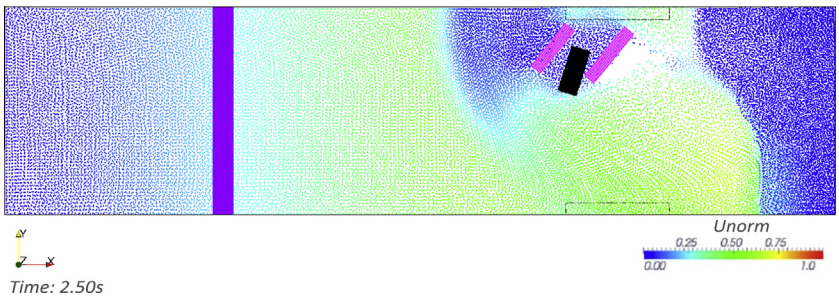

Fig. 9. Dam break with one floating body and two barriers. Time instant of the field of the normalized velocity absolute value – "Unorm" (lateral view).

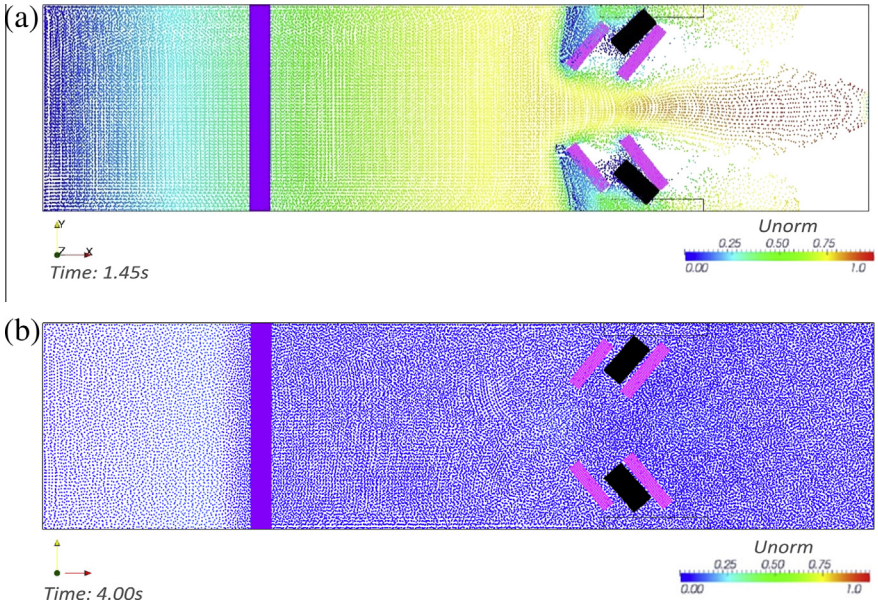

Fig. 10. Dam break with two floating bodies and four barriers. Extract of the time sequence of the field of the normalized velocity absolute value – "Unorm" (lateral view).

limited the intensity of the velocity and, therefore, they constrained the vehicles to move in the area confined by the two groynes. If the incoming flow depth was less than the vehicle height, the velocity intensity should play a major role in the vehicle transport (Teo et al., 2012). The importance of the barrier height on the flood outcomes suggested that this structural configuration could also be useful in pluvial or river floods, where the water depth and the velocity are usually less than in a dam failure event.

Having demonstrated, through a series of diverse configurations, the hydraulic efficiency of the groynes in controlling the movement of one floating body placed in between them, the analysis turned to the efficiency of this control measure in the case of multiple bodies positioned side-by-side along the same side of the road.

In a new configuration, the barriers were only positioned at the beginning and at the end of the idealized vehicle lines parked along each side of the road (see ID configuration no. 3 of Table 1). The results of this simulation show that, in this configuration, the bodies are freer to move (Fig. 11), not being confined in the space between the two barriers. After t = 1.7 s, the bodies, after colliding with each other, were transported by the water flow into the middle of the channel (t = 1.9 s) (Fig. 11) and ultimately downstream (t = 2.5).

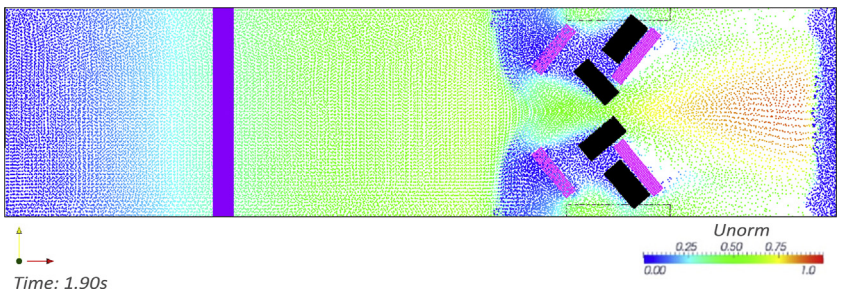

Fig. 11. Dam break with four floating bodies bounded by only one upstream and one downstream barrier to each set of two bodies. Time instant of the field of the normalized velocity absolute value – "Unorm" (lateral view).

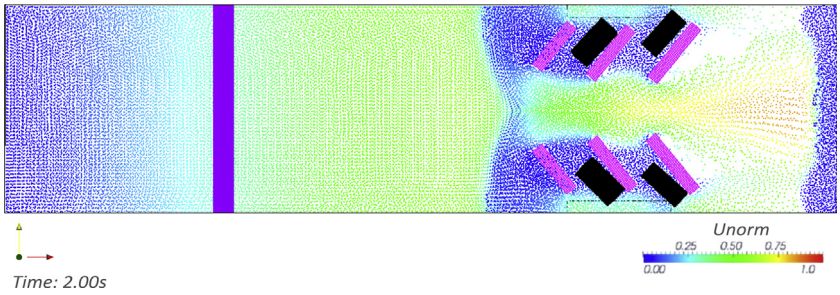

Fig. 12. Dam break with four floating bodies held in individual spaces delimited by groynes. Final time instant of the field of the absolute value of the normalized velocity – "Unorm" (lateral view).

Hence, it was concluded that groynes were only efficient as a mitigation measure if they are positioned upstream and downstream of each body and if they were of at least equal height to the bodies. This was demonstrated in the last simulation (see ID configuration no. 4 of Table 1) in which the bodies remain confined in the spaces delimited by the groynes for the entire duration of the simulation (Fig. 12). The importance of these barriers on the flood outcomes suggests that this structural configuration could also be useful in a pluvial or river flood, where the water depth and the velocity are usually less than in a dam failure event.

5. Conclusions and future work

This research validated the Smoothed Particle Hydrodynamics model of Amicarelli et al. (2015) on 3D complex configurations involving the multiple transport of rigid bodies in free surface flows. The numerical model was tested in a sequence of experimental test cases carried out on a rectangular tilting flume in a laboratory, which simulated the scaled event of a small dam failure involving an urban floodplain with buildings and vehicles in the immediate proximity of the failure. As the numerical model focused on inertial and quasi-inertial fluid flows, neither turbulence scheme nor tangential stresses (simplifying hypothesis) were implemented. Future work is needed to extend the numerical formulation to a wider category of fluid flows. Moreover, the validation of the model needs future work in terms of the pressure field which could be affected by some noise due to the pseudo-compressibility characteristics of the proposed approach. These results could be affected by the number of particles utilized and, thus, an "ensemble" averaging of the pressure field (i.e. obtain the pressure maps at the same time step and average them). In this way, it is possible to improve the pressure field and the impact forces on obstacles.

However, this validation showed the good reliability of the model, in terms of water depth time evolution and time history of the bodies' movements, in reproducing the 3D transport of floating bodies driven by free surface flows, as indicated by the acceptable percentage relative error and Nash–Sutcliffe model efficiency coefficient. Therefore, the model demonstrated that it has reached a level of maturity that allows for quantitative comparison with experimental measurements with accuracy levels similar to those observed in laboratory experiments. Hence, the model could be used to support or eventually substitute laboratory experiments to analyse the impacts of structural mitigation interventions.

The model was applied here in the analysis of the hydraulic efficiency of a proposed flood mitigation structural measure (groynes), in order to evaluate their optimal configuration. Different groynes configurations (see Table 1) were examined in order to identify the most appropriate design and layout for flash-flood damage mitigation, and it was found that the groynes positioned upstream and downstream of each floating body could be an effective risk mitigation measure against damage due to the movement of floating bodies. This result highlighted the potential hydraulic functionality of groynes during flood events.

Obviously, the hydraulic efficiency of the proposed groynes must be tested in more complex idealized configurations, such as in different channel geometries (e.g. curved channels and channels with different inclinations), as well as in a more realistic study (simulation with real street networks). The mitigation measure design proposed in this study was assessed only from the hydraulic point of view and did not take into account civil design and urban planning. Future studies could focus on these issues, in particular on the eco-friendly typologies of material construction (e.g. concrete, metal, etc.), and on civil design methods to reduce the encumbrance of the groynes (i.e. a smaller and more appealing shape). This study does not presume to represent a "ready to use" technology, but rather lays the groundwork for other civil, urban, and environmental design studies aiming to reduce the vulnerability of an urban system during a flooding emergency phase.

The numerical models could also provide an alternative and valuable tool of scientific investigation, providing additional information that cannot be easily obtained from direct experimental observation (Gomez-Gesteira et al., 2010), such as pressure and velocity. In addition, if different engineered (structural and non-structural) options are also taken into account to reduce the impact of disasters, the economic benefits of this form of risk mitigation can include a reduction in the costs incurred by the organizations responsible for managing disaster events and recovery processes (MAFF, 1999; Defra, 2003; Albano et al., 2015). It is important to also highlight the application potential of this model to many different aspects of flood events, including to the transport of solid structures, vehicles, tree trunks, and ice flows, as well as to floating platforms, buoys, and other off-shore situations.

Acknowledgements

We would like to thank two reviewers for their very valuable comments on the initial version of this article. Partial funding for this research was provided by an NSERC Discovery Grant held by Jan Adamowski.

References

Adami, S., Hu, X.Y., Adams, N.A., 2012. A generalized wall boundary condition for smoothed particle hydrodynamics. J. Comput. Phys. 231, 7057–7075.
Adamowski, J., Adamowski, K., Bougadis, J., 2010. Influence of trend on short duration design storms. Water Resour. Manage 24, 401–413.
Albano, R., Mancusi, L., Sole, A., Adamowski, J., 2015. Collaborative strategies for sustainable EU flood risk management: FOSS and geospatial tools—challenges and opportunities for operative risk analysis. ISPRS Int. J. Geo-Inf. 4, 2704–2727.
Anghileri, M., Castelletti, L.M.L., Francesconi, E., Milanese, A., Pittofrati, M., 2011. Rigid body water impact–experimental tests and numerical simulations using the SPH method. Int. J. Impact Eng 38, 141–151.
Amicarelli, A., Albano, R., Mirauda, D., Agate, G., Sole, A., Guandalini, R., 2015. A Smoothed Particle Hydrodynamics model for 3D solid body transport in free surface flows. Comput. Fluids 116, 205–228.

Aureli, F., Dazzi, S., Maranzoni, A., Mignosa, P., Vacondio, R., 2015. Experimental and numerical evaluation of the force due to the impact of a dam-break wave on a structure. Adv. Water Resour. 76, 29–42.
Bouscasse, B., Colagrossi, A., Marrone, S., Antuono, M., 2013. Nonlinear water wave interaction with floating bodies in SPH. J. Fluids Struct. 42, 112–129.
Brodtkorb, A.R., Hagen, T.R., Saetra, M.L., 2013. Graphics processing unit (GPU) programming strategies and trends in GPU computing. J. Parallel Distrib. Comput. 73, 4–13.
Colagrossi, A., Landrini, M., 2003. Numerical simulation of interfacial flows by smoothed particle hydrodynamics. J. Comput. Phys. 191–2, 448–475.
Cox, R.J., Ball, J.E., 2001. Conference on Hydraulics in Civil Engineering, Stability and Safety in Flooded Street. The Institution of Engineers, Hobart, Australia.
Crespo, A.J.C., Gómez-Gesteira, M., Dalrymple, R.A., 2008. Modeling dam break behavior over a wet bed by a SPH technique. J. Waterw. Port Coast. Ocean Eng. 134 (6), 313–320.
Defra, 2003. Revisions to Economic Appraisal Procedures Arising from the New HM Treasury 'Green Book'. Department for Environment, Food and Rural Affairs, London.
Di Monaco, A., Manenti, S., Gallati, M., Sibilla, S., Agate, G., Guandalini, R., 2011. SPH modeling of solid boundaries through a semi-analytic approach. Eng. Appl. Comput. Fluid Mech. 5 (1), 1–15.
Džebo, E., Agar, D., Krzyk, M., Četina, M., Petkovšek, G., 2014. Different ways of defining wall shear in smoothed particle hydrodynamics simulations of a dam-break wave. J. Hydraul. Res. 52 (4), 453–464.
Gimenez, J.M., González, L.M., 2015. An extended validation of the last generation of particle finite element method for free surface flows. J. Comput. Phys. 284, 186–205.
Gómez-Gesteira, M., Dalrymple, R.A., 2004. Using a 3D SPH method for wave impact on a tall structure. J. Waterw. Port Coast. Ocean Eng. 130 (2), 63–69.
Gomez-Gesteira, M., Rogers, B.D., Violeau, D., Grassa, J.M., Crespo, A.J.C., 2010. Foreword: SPH for free-surface flows. J. Hydraul. Res. 48 (1), 3–5.
Gonzalez, R.C., Woods, R.E., 2008. Digital Image Processing. Pearson International Edition.
Grimaldi, A., Sollo, A., Guida, M., Marulo, F., 2013. Parametric study of a SPH high velocity impact analysis – a birdstrike windshield application. Compos. Struct. 96, 616–630.
Gruntfest, E., Ripps, A., 2000. Flash floods: warning and mitigation efforts and prospects. In: Parker, D. (Ed.), Floods, vol. 1. Routledge, London, pp. 377–390.
Gruntfest, E., 1997. What people did during the Big Thompson flood. Working Paper No. 32. Natural Hazard Center, Boulder.
Gruntfest, E., 2000. Flash floods in the United States. In: Pielke, J.R., Pielke, S.R. (Eds.), Storms. Routledge, London, pp. 192–206.
Halbe, J., Pahl-Wostl, C., Sendzimir, J., Adamowski, J., 2013. Towards adaptive and integrated management paradigms to meet the challenges of water governance. Water Sci. Technol.: Water Supply 67, 2651–2660.
Hashemi, M.R., Fatehi, R., Manzari, M.T., 2011. SPH simulation of interacting solid bodies suspended in a shear flow of an Oldroyd-B fluid. J. Nonnewton. Fluid Mech. 166, 1239–1252.
Hashemi, M.R., Fatehi, R., Manzari, M.T., 2012. A modified SPH method for simulating motion of rigid bodies in Newtonian fluid flows. Int. J. Non-Linear Mech. 47, 626–638.
Idelsohn, S.R., Oñate, E., Pin, F. Del, 2004. The particle finite element method: a powerful tool to solve incompressible flows with free-surfaces and breaking waves. Int. J. Numer. Meth. Eng. 61, 964–989.
Inam, A., Adamowski, J., Halbe, J., Prasher, S., 2015. Using causal loop diagrams for the initialization of stakeholder engagement in soil salinity management in agricultural watersheds in developing countries: A case study in the Rechna Doab watershed. Pakistan. J. Environ. Manage. 152, 251–267.
Kajtar, J.B., Monaghan, J.J., 2010. On the dynamics of swimming linked bodies. Eur. J. Mech. B/Fluids 29, 377–386.
Kajtar, J.B., Monaghan, J.J., 2012. On the swimming of fish like bodies near free and fixed boundaries. Eur. J. Mech. B/Fluids 33, 1–13.
Keller, R.J., Mitsch, 1993. Safety Aspects of the Design of Roadways as Floodways, Research Report No. 69. Urban Water Research Association of Australia.
Kolinjivadi, V., Adamowski, J., Kosoy, N., 2014. Recasting payments for ecosystem services (PES) in water resource management: a novel institutional approach. Ecosyst. Services 10, 144–154.
Lucìa, A., Comiti, F., Borga, M., Cavalli, M., Marchi, L., 2015. Dynamics of large wood during a flash flood in two mountain catchments. Nat. Hazards Earth Syst. Sci. 15, 1741–1755.
Liu, G.R., Liu, M.B., 2003. Smoothed Particle Hydrodynamics: A Meshfree Particle Method. World Scientific, ISBN 981-238-456-1.
Liu, X., Xu, H., Shao, S., Lin, P., 2013. An improved incompressible SPH model for simulation of wave structure interaction. Comput. Fluids 71, 113–123.
Liu, M.B., Shao, J.R., Li, H.Q., 2014. An SPH model for free surface flows with moving rigid objects. Int. J. Numer. Meth. Fluids 74 (9), 684–697.
MAFF, 1999. Flood and Coastal Defence Project Appraisal Guidance (3): Economic Appraisal. Ministry of Agriculture, Fisheries and Food, London.
McCarthy, M.A., Xiao, J.R., McCarthy, C.T., Kamoulakos, A., Ramos, J., Gallard, J.P., Melito, V., 2004. Modelling of bird strike on an aircraft wing leading edge made from fibre metal laminates – Part 2: modelling of impact with SPH bird model. Appl. Compos. Mater. 11 (5), 317–340.
McKenna, F., Fenves, G.L., Scott, M.H., 2000. Open system for Earthquake Engineering Simulation. University of California, Berkeley, CA. Available from: <http://opensees.berkeley.edu>.
Mirauda, D., Greco, M., Volpe Plantamura, A., 2011. Influence of the entropic parameter on the flow geometry and morphology. In: Proceedings of International Conference on Water, Energy and Environment, Phuket, Thailand, pp. 1357–1362.
Mirauda, D., Volpe Plantamura, A., Malvasi, S., 2013. Boundaries influence on the flow field around an oscillating sphere. In: ASME 2013 32nd International Conference on Ocean, Offshore and Arctic Engineering.
Monaghan, J.J., 2005. Smoothed particle hydrodynamics. Rep. Prog. Phys. 68, 1703–1759.
Monaghan, J.J., Kos, A., Issa, N., 2003. Fluid motion generated by impact. J. Waterw. Port Coast. Ocean Eng. 129, 250–259.
Nalley, D., Adamowski, J., Khalil, B., Ozga-Zielinski, B., 2013. Trend detection in surface air temperature in Ontario and Quebec, Canada during 1967–2006 using the discrete wavelet transform. J. Atmos. Res. 132 (133), 375–398.
Nash, J.E., Sutcliffe, J.V., 1970. River flow forecasting through conceptual models Part I—a discussion of principles. J. Hydrol. 10 (3), 282–290.
Nourani, V., Baghanam, A., Adamowski, J., Kisi, O., 2014. Applications of hybrid wavelet-artificial intelligence models in hydrology: a review. J. Hydrol. 514, 358–377.
Omidvar, P., Stansby, P.K., Rogers, B.D., 2012a. Wave body interaction in 2D using smoothed particle hydrodynamics (SPH) with variable particle mass. Int. J. Numer. Meth. Fluids 68, 686–705.
Omidvar, P., Stansby, P.K., Rogers, B.D., 2012b. SPH for 3D floating bodies using variable mass particle distribution. Int. J. Numer. Meth. Fluids. http://dx.doi.org/10.1002/fld.3749.
Onate, E., Idelsohn, S.R., Del Pin, F., Aubry, R., 2004. The particle finite element method – an overview. Int. J. Comput. Methods 01, 267.
Onate, E., Celigueta, M.A., Idelshon, S.R., Suarez, F.S.B., 2011. Possibilities of the particle finite element method for fluid–soil–structure interaction problems. Comput. Mech. 48, 307–318.
Onate, E., Celigueta, M.A., Latorre, S., Casas, G., Rossi, E., Rojek, J., 2014. Lagrangian analysis of multiscale particulate flows with the particle finite element method. Comput. Part. Mech. 1, 85–102.
Pacejka, H.B., 2005. Tyre and Vehicle Dynamics. Elsevier Science & Technology.
Pingale, S., Khare, D., Jat, M., Adamowski, J., 2014. Spatial and temporal trends of mean and extreme rainfall and temperature for the 33 urban centres of the arid and semi-arid state of Rajasthan, India. J. Atmos. Res. 138, 73–90.
Razavitoosi, S.L., Ayyoubzadeh, S.A., Valizadeh, A., 2014. Two-phase SPH modelling of waves caused by dam break over a movable bed. Int. J. Sedim. Res. 29 (3), 344–356.
Ren, B., Jin, Z., Gao, R., Wang, Y.-X., Xu, Z.-L., 2014. SPH–DEM modeling of the hydraulic stability of 2D blocks on a slope. J. Waterw. Port Coast. Ocean Eng. 140 (6).
Ren, B., He, M., Dong, P., Wen, H., 2015. Nonlinear simulations of wave-induced motions of a freely floating body using WCSPH method. Appl. Ocean Res. 50, 1–12.
Seungtaik, O., Younghee, K., Byung-Seok, R., 2009. Impulse-based Boundary Force (IBF). Comput. Anim. Virtual Worlds 20, 215–224.
Shu, C., Xia, J., Falconer, R.A., Lin, B., 2011. Incipient velocity for partially submerged vehicles in floodwaters. J. Hydraul. Res. 49 (6), 709–717.
Simon, D., 2006. Optimal State Estimation: Kalman, H Infinity, and Nonlinear Approaches. Wiley.
Soares-Frazão, S.A., Zech, Y., 2007. Experimental study of dam-break flow against an isolated obstacle. J. Hydraul. Res. 45 (1), 27–36.
Straith, D., Adamowski, J., Reilly, K., 2014. Exploring the attributes, strategies and contextual knowledge of champions of change in the Canadian water sector. Can. Water Resour. J. 39 (3), 255–269.
Sun, P., Ming, F., Zhang, A., 2015. Numerical simulation of interactions between free surface and rigid body using a robust SPH method. Ocean Eng. 98, 32–49.
Teo, F.Y., Xia, J., Falconer, R.A., Lin, B., 2012. Experimental study on the interaction between vehicles and floodplain flows. Int. J. River Basin Manage. 10 (2), 149–160.
Vacondio, R., Rogers, B.D., Stansby, P.K., 2012. Accurate particle splitting for smoothed particle hydrodynamics in shallow water with shock capturing. Int. J. Numer. Meth. Fluids 69, 1377–1410.
Vacondio, R., Dal Palù, A., Mignosa, P., 2014. GPU-enhanced Finite Volume Shallow Water solver for fast flood simulations Environmental. Modell. Softw. 57, 60–75.
Vaughan, G.L., 2009. The SPH equations for fluids. Int. J. Numer. Meth. Eng. 79, 1392–1418.
Viccione, G., Bovolin, V., Carratelli, E.P., 2008. Defining and optimizing algorithms for neighbouring particle identification in SPH fluid simulations. Int. J. Numer. Meth. Fluids 58, 625–638.
Viccione, G., Bovolin, V., 2011. Simulating triggering and evolution of debris-flows with SPH. Proceedings of the 5th International Conference on Debris-Flow Hazards Mitigation: Mechanics, Prediction and Assessment. Italian J. Eng. Geol. Environ. 03, 523–532.
Violeau, D., 2012. Fluid Mechanics and the SPH Method – Theory and Applications. Oxford University Press, ISBN-10: 0199655529.
Xia, J., Teo, F.Y., Lin, B., Falconer, R.A., 2011a. Formula of incipient velocity for flooded vehicles. Nat. Hazards 58, 1–14.
Xia, J., Falconer, R.A., Lin, B., Tan, G., 2011b. Numerical assessment of flood hazard risk to people and vehicles in flash flood. Environ. Modell. Softw. 26, 987–998.
Zhang, X., Krabbenhoft, K., Sheg, D., Li, W., 2015. Numerical simulation of a flow-like landslide using the particle finite element method. Comput. Mech. 55, 167–177.
Zhu, M., Scott, M.H., 2014. Modeling fluid–structure interaction by the particle finite element method in OpenSees. Comput. Struct. 132, 12–21.